Modeling, Design, and Experimental Evaluation of Rotational Elastic Joints for Underactuated Robotic Fingers

Umberto Scarcia[†1], Giovanni Berselli [‡2], Gianluca Palli[†3], Claudio Melchiorri[†4]

Abstract— In this paper, a novel 3D printed Rotational Joint (RJ) embedding an integrated elastic element is presented. The RJ, produced as a single piece by means of an FDM printer, comprises a traditional pin hinge coupled with a pair of spiral torsion springs, providing the desired compliance for the application at hand. Benefits of the proposed design include monolithic manufacturing and possibility to be successfully employed in robotic articulated devices requiring joint elasticity for their functioning. On the other hand, the sub-optimal RJ behavior, mainly caused by the unavoidable friction between 3D printed mating surfaces, must be accurately taken into account for design purposes. In this context, preliminary reliability tests have been performed showing promising results in terms of lifetime and negligible fatigue effects. Then, a mathematical model of the system is derived, which comprises the spring elasticity along with any frictional effects that may be due to either the pin hinge itself or the tendon transmission (frequently employed in underactuated robotic devices). The model parameters have been empirically evaluated by comparing simulated and experimental data. In addition, the last part of the paper describes how the proposed RJ can be effectively employed for the design of modular, underactuated fingers, providing three degrees of freedom and a single tendon transmission. To this end the model of the joint module proposed in this work will be the starting point for the geometry dimensioning of a finger with a desired free closure motion.

I. INTRODUCTION

The actual trend in the field of robotic finger design is to conceive solutions that exploit modern production technologies in order to obtain devices that are relatively inexpensive, simple to produce, assembly/maintain and, on the other hand, durable, robust and easily customizable to the specific application. For instance, when a robotic gripper is designed for purely grasping tasks (i.e. no need of advanced in-hand manipulation capabilities), underactuation may be envisaged as one of the most promising way to achieve these goals [1], [2]. As widely known in the scientific community, underactuation basically means that an articulated structure is realized so as to provide more degrees-of-freedom (*dof*) than degrees-of-actuation (*doa*). In this case, each finger joint cannot be independently controlled and the overall gripper kinematic/dynamic behavior depends on the external load applied to the fingers. In the literature, we can find a great number of attempts to effectively design underactuated devices. In particular, one can find solutions in which the coupling of the phalanges is achieved by means of articulated mechanisms such as four-bar linkages [3], belts [4], or
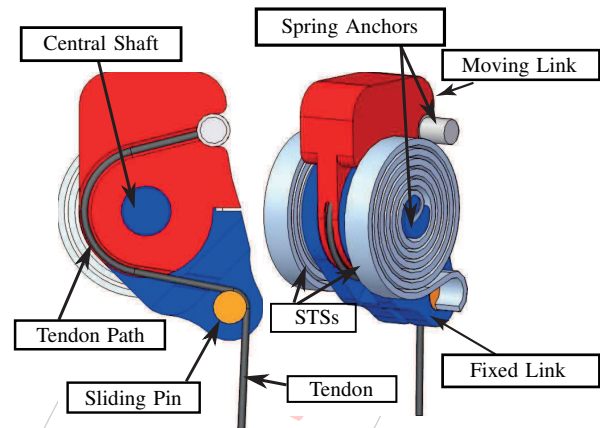

Fig. 1.   Rotational joint with integrated spiral torsion spring

cables routed on pulleys [5]. The use of elastic elements between phalanges is also quite common [6]–[8]. This solution reduces the capability to exert forces or to achieve high velocities in some directions (typically the extension of the finger), but represents an effective way to reduce the number of actuators. This approach is quite popular and we can find many different past solutions that comprise interphalangeal elasticity. For instance, joint compliance may be achieved by using classical compression or traction helicoidal springs [9], [10], flexible structures developed with the same material of the phalanges by properly shaping the material in proximity of the articulation [12], multi-material compliant mechanisms with the integration of soft rubber-like parts between the two links [13]. Similarly to the cited literature, in this work, we are interested in investigating the use of rapid prototyping technology to produce monolithic joint modules with an embedded elastic component. When connected in series, these modules can be used to design, for instance, a robotic finger. The idea is to exploit the intrinsic elasticity of ABS plastics used in FDM (Fused Deposition Modeling) to design a Spiral Torsion Spring (STS) that can be produced together with the joint in one single production step. The main problems found in the previous works that follow similar approaches are the low material Yield strength and the rather poor fatigue life. However, the great flexibility of design given by modern 3D printing techniques allows to carefully optimize the morphology of the compliant element and, therefore, improve the RJ performance and lifetime. In our previous studies [14], we have shown how analytic models used to design common spiral springs can be adopted also when optimizing ABS-based STS. The

† Dept. of Electrical Electronic and Information Engineering "Guglielmo Marconi", University of Bologna, Italy. ‡ Dept of Mechanics, Energetics, Management and Transportations, University of Genova, Italy. Email: [1]*umberto.scarcia2@unibo.it,*   [2]*giovanni.berselli@unige.it*   [3]*gianluca.palli@unibo.it,* [4]*claudio.melchiorri@unibo.it.*

proposed model, given the specification of the material along with requirements on the desired stiffness and maximum rotational displacement, allows to select a set of geometric parameters that can be used to generate the spring 3D model ready to be printed. Building upon these assumptions, in the following, we present how these ABS-based STS can be employed for the implementation of monolithic RJ modules, which are then employed for fabricating a tendon-actuated robotic finger manufactured in a single production step. In addition, the effect of friction loads arising in the RJ during its motion are described via mathematical relations whose parameters are determined through a series of experimental tests. This paper is organized as follows: Sec. II recalls the analytic model used to select the geometric parameters of the desired spring; Sec. III reports about the joint module with integrated compliant element, along with preliminary tests for failure analysis; Sec. IV shows an RJ mathematical model that takes into account the stiffness of the spring and the friction effects of both revolute sliding pairs and tendon transmission; Sec. V reports about experimental tests, whereas Sec. VI summarizes the outcomes and the future developments.

II. BACKGROUND ON STS MODELING AND DESIGN

STSs are generally manufactured employing medium/carbon steel alloys shaped as thin rods with rectangular section bent along a central axis. They are used when relatively low stiffness and high angular deformations are required. The analytic model of STSs is widely discussed in the mechanical design literature [15], [16]. With reference to Fig. 2, the relation between the torque and the angular deformation at the central shaft is a non linear function of dimensional parameters and material Young's modulus.

The torque T generated by the spring deformation $\Delta\theta$ and acting about the z axis can be easily described as:

$$T = K(b, t, L_e)\,\Delta\theta \qquad (1)$$

$$K(b, t, L_e) = \frac{E\,b\,t^3}{12\,L_e} \qquad (2)$$

where $K(b, t, L_e)$ is the STS stiffness, expressed as a function of the spring geometric parameters, the constants E and L_e being respectively the material Young's modulus and the effective spiral length interested by the deformation. It is
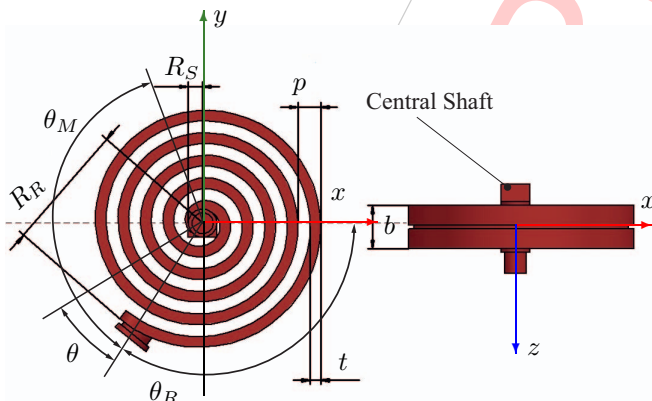

Fig. 2.   Spring geometric parameters.

interesting to note that the torsional spring stiffness does not depend on the shape of the spiral (i.e. the external radius, the pitch between coils or the number of turns), but only on the geometric parameters of the rod, namely b, t and L_e. In [14] we propose an optimization algorithm that computes the STS parameters achieving a desired stiffness, minimum encumbrance, and producing a stress along the spring (at the maximum required deformation) that does not exceed the Yield stress of the material.

III. JOINT DESIGN AND LIFETIME ASSESSMENT

The main design goal is to conceive a RJ that can be possibly manufactured in one single step via 3D printing, without the need of assembling any external parts (such as shafts, bearings or screws). The RJ comprises an integrated STS that provides a restoring torque allowing the joint to reach its fully extended configuration whenever no external loads are applied. In addition, the RJ is designed as a *modular* element, meaning that multiple modules can be effectively connected in series, thus obtaining a structure that acts as an underactuated finger driven in its motion by a single tendon. Therefore, the spring shall be characterized by a rather low stiffness constant, since only frictional and gravitational forces need to be overcome in order to guarantee the RJ full extension whenever the tendon tension is released. Owing to these basic observations, the effect of both friction and weight of the phalanges needs to be carefully taken into account during the design phase. In parallel, a successful STS integration within the RJ implies a limited spring encumbrance, hence limiting the overall dimensions of the device. The design solution proposed consists of knuckle joint and a couple of STSs symmetrically placed on the RJ external sides. The STSs are basically anchored on the knuckle pin integrated in the ground link, on one end, and constrained on a couple of cylindrical protrusions integrated in the moving link, on the other end. As it can be seen from Fig. 1 (and, successively, in Fig. 7(b)), the spring is manufactured in such a way that it can be preloaded at the rest position of the joint. The possibility for preloading is achieved by designing the termination of the spring not in correspondence of the connection pin located on the mobile link, but with an angular offset along the extension direction. In this case, a preload of 90 deg is introduced. The cable is routed on a sliding path directly obtained on the eye end of the knuckle joint and on a cylindrical support (orange pin) located on the moving (red) link. Fork, eye and pin composing the knuckle joint are manufactured together, without the need of further assembly. This is possible by properly dimensioning the free space between the ground and moving links shown in Fig. 1. The integrated knuckle joint allows the motion of the mobile link along the primary axis only, whereas all the secondary directions are mechanically constrained at the expense of friction generation due to the sliding mating surfaces. Also in this case, the dimensioning of the free space between the two links plays a crucial role in order to mitigate frictional effects. With the 3D printer used for this work (Stratasys Dimension Elite), we

TABLE I
PRELIMINARY FAILURE ANALYSIS AS FUNCTION OF STS DESIGN
PARAMETERS (ROD WIDTH, $b = 4.8mm$).

Design Alternative #C				
Spiral Length	*Pitch*	*Rod Thickness*	*Pin Backlash*	**Cycles to failure**
264.81mm	1.6mm	1mm	0.25mm	4.0e5
264.81mm	1mm	0.8mm	0.25mm	4.9e5
142.72mm	1.67mm	0.8mm	0.75mm	3.0e4
138.03mm	1.67mm	1mm	0.75mm	4.0e4
410.31mm	1mm	0.5mm	0.75mm	2.3e4
410,31mm	1mm	0.5mm	0.25mm	1.2e5
292.32mm	1.6mm	1mm	0.25mm	over 8.5e5

experienced that a backlash of 0.25 mm is enough to produce two parts that are well separated after the suppression of the support sacrificial material (commonly employed in additive manufacturing).

Preliminary Failure Analysis: A major issue which usually advises against the use of 3D printing as an effective production technology is poor material reliability. At present, several FDM plastics are commercially available (e.g. PLA and Ultem 9085 [17]), materials with higher S_y/E ratio being preferable when realizing compliant mechanisms [18]. In the present paper, owing to its wide-spread employability in several 3D printers, ABSplus-P430 has been chosen as one possible solution. The basic material constitutive parameters can be found on the supplier datasheets [19].

Nonetheless, typical flexure hinges (i.e. beam-like flexures), would surely fail if ABS is employed and large deflections are required. On the other hand, in case of STSs, a careful selection of the spring geometric parameters allows to obtain reliable design solutions which are fully appropriate for usage in small-scale gripping devices. In particular a set of preliminary tests has been carried out in order to determine the RJ lifetime in applications requiring about 90 deg rotations, the RJ being continuously operated at a constant speed of 30 cycles per minute up to mechanical failure. Preliminary results are reported in Tab. I, which highlights that a poorly designed STS fails rather quickly, whereas optimized design can exceed 8.5e5 cycles without failure.

IV. JOINT CHARACTERIZATION

In this section, the joint implemented exploiting the designed spring has been characterized by means of a proper set of experimental tests, as reported in Fig. 3. This characterization aims at providing information for the control not just of a single joint, but of a whole robotic finger, developed hereafter.

The joint has been mounted with the fixed link connected to an ATI Gamma SI-130-10 F/T sensor, as it can be seen in Fig. 3(b), where a schematic representation of the measurement setup is shown. In parallel, the moving link has been moved by means of a rotating bar. For measuring the joint deflection, a couple of markers have been applied to both base and moving links, as shown in Fig. 3(a), and a camera placed above the joint has been used to detect the marker positions and, therefore, the relative angular position of the two links (i.e. the joint deflection). In Fig. 4(a), the angle-torque relation provided by the joint during this test is reported. During this first experiment, the torque acting on the joint and measured by the ATI F/T sensor is generated by the friction of the joint pins and by the springs elastic torque. It is important to note that the bar mounted on the moving link, other than allowing an easier motion of the joint, applies also to the link a transverse load of 0.1 N at a distance of 70 mm from the joint axis (due to the weight of the bar itself). This transverse load is applied to amplify the effect of the joint friction, that is otherwise difficult to appreciate, as it will also be highlighted during the following experiments.

From Fig. 4(a) it can be noted that the joint angle-torque relation is clearly given by the superposition of two distinct effects: the joint spring stiffness and the static joint friction. Despite the available friction models, in the case here presented, a simple Coulomb static friction model can be used to describe the joint friction. With reference to Fig. 4(a), the upper red dashed line and the bottom blue one represent the positive (i.e. in case of positive joint velocity) friction level and the negative (i.e. in case of negative joint velocity) friction level respectively, whereas the green dashed line has been obtained as the mean value between the offset and the slope of the red and blue lines. For the data interpolation of the experiment shown in Fig. 4, the positive and negative cycles have been identified by segmenting the torque data corresponding to positive and negative velocity respectively, and by applying filtering windows over 10 data samples to eliminate the transition between the two phases (the vertical part of the plot). This test also confirms that the joint friction can be modeled by means of a symmetric Coulomb model, namely:

$$\tau_j = \begin{cases} K_s\,\theta + \mu_j F_n, & \dot{\theta} > 0 \\ K_s\,\theta - \mu_j F_n, & \dot{\theta} < 0 \end{cases} \quad (3)$$

where τ_j is the torque needed to move the joint, K_s is the spring stiffness, $\theta = \theta_j + \theta_0$ is the overall spring deformation, with θ_j and $\theta_0 = 70$ deg being respectively the effective joint rotation angle and the spring preload, μ_j is the generalized joint friction coefficient (we refer to a generalized friction coefficient since it relates linear and rotational quantities and, therefore, it is not adimensional), and F_n is the external load acting on the joint. It can be noted that the green dashed line passes through the zero torque value for a null spring deformation angle, and that its slope corresponds to $K_s = 5.19$ N mm/rad, that fits very well with the designed spring stiffness, i.e. 5.2 N mm/rad. Due to the joint geometry, the external load acting on the joint during this test can be quantified in $F_n = 1.5$ N. Therefore, by considering a mean Coulomb friction level provided by this experiment of 10.39 N mm, a generalized friction coefficient $\mu_j = 6.92$ mm is obtained.

To further verify the joint model proposed in Eq. (3), a set of four experiments have been performed, in which the joint has been actuated by a tendon. The tendon adopted during
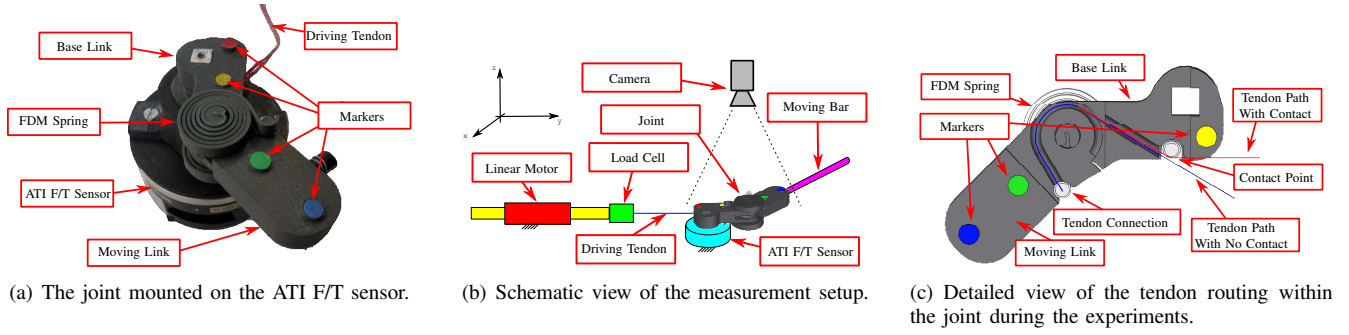
(a) The joint mounted on the ATI F/T sensor.

(b) Schematic view of the measurement setup.

(c) Detailed view of the tendon routing within the joint during the experiments.

Fig. 3. Detailed view and schematic representation of the joint characterization setup and tendon routing inside the base link.

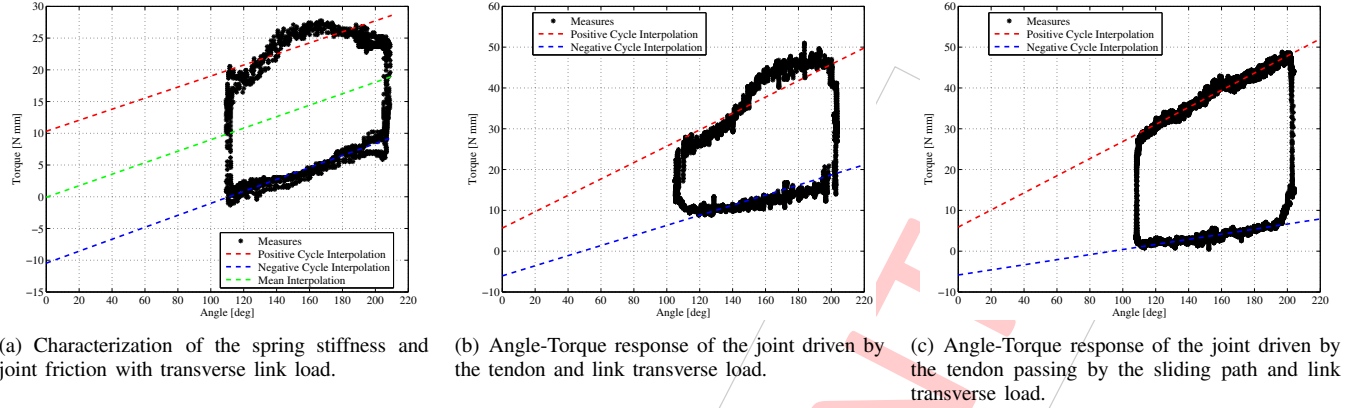(a) Characterization of the spring stiffness and joint friction with transverse link load.

(b) Angle-Torque response of the joint driven by the tendon and link transverse load.

(c) Angle-Torque response of the joint driven by the tendon passing by the sliding path and link transverse load.

Fig. 4. Characterization of the joint displacement-torque relation in case of transverse joint load.

the experiments is a DynaFLIGHT 97 Dyneema Bowstring, characterized by low creep and low surface friction. In the first test, whose results are reported in Fig. 4(b), the tendon driving the joint is not routed along the path inside the base link to avoid introducing additional friction effects due to the contact between the tendon and the link itself (see Fig. 3(c) where the detail of the tendon routing within the joint during the experiment is shown). In parallel, the transverse joint load is the same as the test shown in Fig. 4(a). This experiment allows to evaluate that, despite the friction effect due to the load generated on the joint by the tendon (this effect will be further clarified by a dedicated experiment in the following), the spring stiffness and joint friction effects are maintained, as it can be seen, in particular, by the projection of the interpolating dashed lines reported in this plot. In the second experiment, whose results are reported in Fig. 4(c), the transverse joint load is kept as in the previous test and the tendon driving the joint is routed along the path inside the base link, so that the friction effects due to the contact between the tendon and the link is highlighted. Also in this case, despite the additional friction induced by the tendon contact with the link, the spring stiffness and joint friction effects are also maintained in this plot, as the interpolating dashed lines show.

In the third and forth experiment, the transverse joint load has been removed to highlight the effects introduced by the tendon. In particular, the experiment shown in Fig. 5 reproduces the same condition of the test in Fig. 4(b), but without the joint transverse load, allowing to appreciate the effect of the friction induced by the tendon load on the joint itself. This effect can be explained considering that, due to

the joint structure, the tendon does not apply a pure torque on the joint, but applies a force that is converted into a torque by the joint pulley used to route the tendon. Moreover, the force applied by the tendon for moving the joint increases with the joint deflection, because of the torque generated by the spring. These combined effects result in a joint pin load and a consequent friction, caused by the tendon and proportional to the joint deflection. Therefore, assuming that in this experiment $F_n = 0$ and considering that now the joint is driven by the tendon, the model of Eq. (3) can be extended in the following way:

$$\tau_j = r\, F_t = \begin{cases} (K_s + \gamma^+)\,\theta + \mu_j F_n, & \dot\theta > 0 \\ (K_s - \gamma^-)\,\theta - \mu_j F_n, & \dot\theta < 0 \end{cases} \quad (4)$$

where r is the radius of the joint driving pulley, γ^+ and γ^- represent the positive ($\dot\theta > 0$) and negative ($\dot\theta < 0$) generalized joint friction coefficient of the tendon-induced friction respectively, and F_t is the tendon force. For this model, it results that this friction affects the apparent joint stiffness. Exploiting the previous value of K_s given by the experiment in Fig. 4(a), the spring stiffness can be removed from the measure reported in the top plot of Fig. 5, in order to isolate the value of γ^+ and γ^-, as reported in the bottom plot of Fig. 5 where the terms $\gamma^+ \theta$ and $\gamma^- \theta$ are shown during the positive ($\dot\theta > 0$) and negative ($\dot\theta < 0$) joint movements. From the experimental data, it results $\gamma^+ = 1.89\,\mathrm{N\,mm/rad}$ and $\gamma^- = 3.15\,\mathrm{N\,mm/rad}$. Also in this experiment, the data have been segmented using the same approach adopted for the plots in Fig. 4. It is also worth mentioning that the difference between γ^+ and γ^- can be imputed to the fact that during the positive cycle, the tendon generated torque is opposite
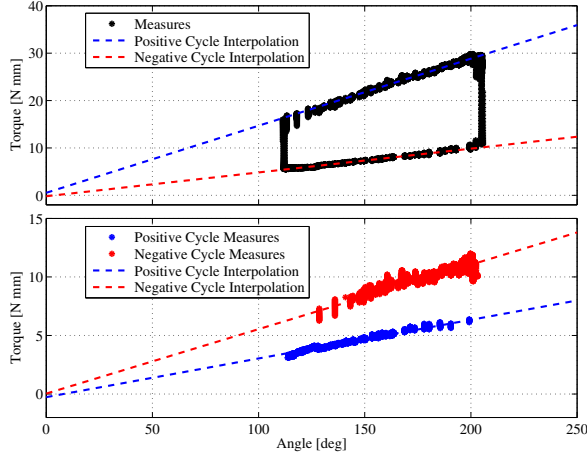
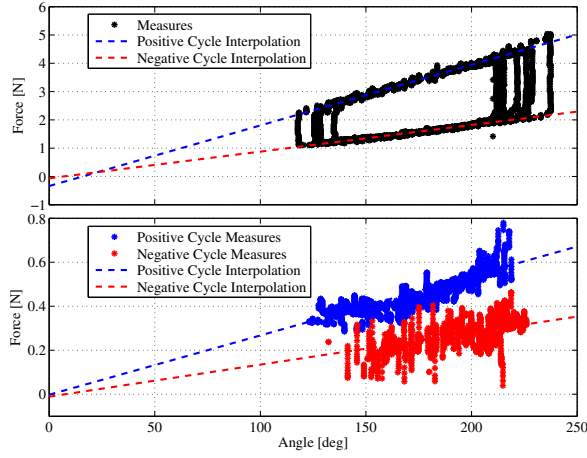Fig. 5. Characterization of the joint friction induced by the tendon load.

Fig. 6. Characterization of the tendon friction generated by the contact with the tendon path.

to the friction and joint spring torque. On the other hand, during the negative cycle, the friction torque only changes direction, so that the tendon load decrease significantly and, consequently, the joint load decreases as well.

In the last experiment, reported in Fig. 6, the joint has been evaluated without the external load but with the tendon sliding on the path inside the base link, therefore generating additional friction along the tendon. This additional friction effects have been extensively studied in [20]. Summarizing the literature results, the friction generated by the tendon contact with the base link can be modeled as

$$F_f = \begin{cases} F_t(1 - e^{\mu_t \alpha}), & \dot{\theta} > 0 \\ F_t(1 - e^{-\mu_t \alpha}), & \dot{\theta} < 0 \end{cases} \quad (5)$$

where F_f is the friction acting on the tendon, μ_t is the tendon generalized friction coefficient over the sliding surface (on the base link) and α is the total tendon curvature angle generated by the contact. In this model, it is also assumed that the velocity of the tendon is positive during the joint positive movements (i.e. when $\dot{\theta} > 0$) and negative during negative joint movements (i.e. when $\dot{\theta} < 0$). Since, due to the characteristics of the joint, the parameters μ_t and α can be considered constant, the model of Eq. (5) can be rewritten
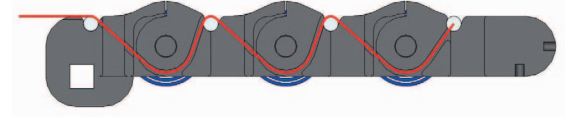
(a) The routing of the tendon within the finger.

(b) The modular monolithic 3D printed finger.

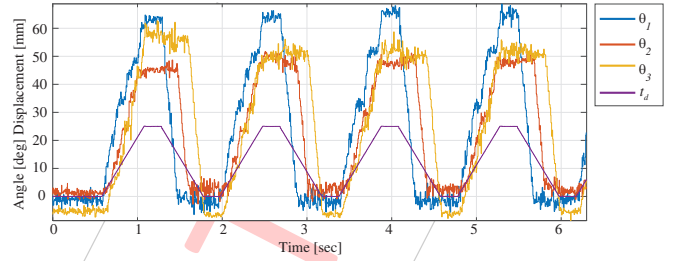Fig. 7. Modular monolithic finger design and prototype

Fig. 8. Response of the finger to tendon actuation.

as

$$F_f = \begin{cases} F_t(1 - \beta^+), & \dot{\theta} > 0 \\ F_t(1 - \beta^-), & \dot{\theta} < 0 \end{cases} \quad (6)$$

where, $\beta^+ = e^{\mu_t \alpha}$ and $\beta^- = e^{-\mu_t \alpha}$. Since in this test the focus is on the tendon friction, the tendon driving force with respect to the joint deflection is plotted in the top plot of Fig. 6. Moreover, by removing the effects described by the previous experiments (and summarized by the model of Eq. (4)) from these measurement, the effect of the friction on the tendon can be isolated and the value of the coefficients β^+ and β^- can be estimated, as shown in the bottom plot of Fig. 6. Therefore, considering the reduction of the tendon force acting on the joint caused by the tendon friction, the model of Eq. (4) can be extended to account for this additional phenomenon. In particular, the following relation hold:

$$\tau_j = r \left(F_t - F_f\right) \\ = \begin{cases} F_t \beta^+ = (K_s + \gamma^+) \theta + \mu_j F_n, & \dot{\theta} > 0 \\ F_t \beta^- = (K_s - \gamma^-) \theta - \mu_j F_n, & \dot{\theta} < 0 \end{cases} \quad (7)$$

From the experimental data reported in the bottom plot of Fig. 6, it results $\beta^+ = 1.24$ and $\beta^- = 0.67$. Also in this experiment the data have been segmented using the same approach adopted for the plots in Fig. 4.

V. THE MODULAR UNDERACTUATED FINGER

To practically demonstrate the effectiveness of the proposed compliant joint, a modular articulated finger has been designed and prototyped. The finger is composed of four links, namely the base, proximal, medial and distal phalanges. Each revolute pair consists of a RJ module as described in the previous sections. As depicted in Fig. 7(a), which shows a section view of the finger CAD model,
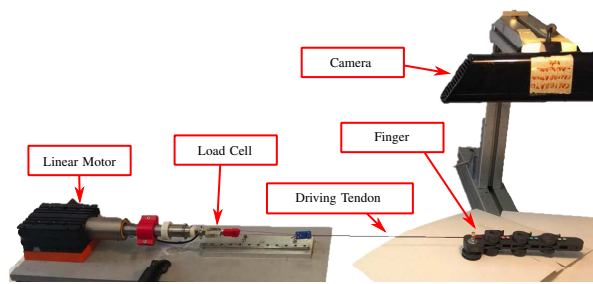
(a) The setup used to test the finger behavior.

Fig. 9. Experimental finger setup and finger behavior with different contact locations.

only one tendon is used for actuation. The length of each link is set to 40 mm, whereas the STS used for the three joints are characterized by different stiffness constants. In particular, $K_{s1}=K_s$, $K_{s2}=1.5\,K_s$ and $K_{s3}=2\,K_s$, where K_s =5.2 N mm/rad and the subscript $i = 1, 2, 3$ are related to either the proximal, medial and distal RJ. This particular choice allows to compensate for the different gravitational components due to the weight of the links on the three joints and allows to keep the finger extended when the tendon is completely relaxed.

An experimental set-up has been implemented in order to preliminary analyze the behavior of the finger. At this stage we are interested in observing the finger motion when the tendon is pulled and no contact arises on the surface of the finger. A position controlled linear motor is used to pull the tendon while a vision tracker records the joint angles of the finger during its motion. In Fig. 8, the behavior of the three joint angles, θ_1, θ_2, θ_3, corresponding to a tendon displacement t_d ranging from 0 to 25 mm is shown. It is interesting to note the clear effect of friction. The proximal joint is the first that starts to move under the effect of the tendon tension. When the joints moves, the tension of the tendon reaches the second and third joint that start to move almost simultaneously. At the end of the stroke of the linear motor, the joints angular displacements are, respectively, $\theta_1 = 65$, $\theta_2, \theta_3 = 50$.

VI. Conclusions

In this paper, a 3D printed rotational elastic joint suitable to be used as a module for the development of underactuated robotic hands has been presented. It has been tested in order to empirically determine the number of loading cycles leading to failure. These preliminary reliability tests show the potential of this type of joint for real applications. Secondly, a mathematical model of the joint behavior has been developed, including friction effects deriving from the tendon actuation. These models have been validated with an extensive laboratory activity (in order to empirically determine the model parameters). Finally, as an example of possible devices that could be designed using these modules, an underactuated finger has been illustrated. The results achieved so far are quite promising for the design of reliable, low-cost robotic articulated devices requiring joint elasticity for their functioning. Future work will deal with the

evaluation of the maximum bearable secondary loads along with the design and production of a robotic multi-fingered device for grasping and simple manipulation tasks.

Appendix: Index to Multimedia Extensions

The video attachment shows the four experiments carried out during the RJ characterization along with the behavior of an underactuated finger in different contact scenarios.

Acknowledgment

References

[1] L. Birglen, T. Laliberté, and C. M. Gosselin, *Underactuated Robotic Hands*. Springer Berlin, 2008.

[2] X. Xin and Y. Liu, *Control Design and Analysis for Underactuated Robotic Systems*. Springer London, 2014.

[3] K. Telegenov, Y. Tlegenov, and A. Shintemirov, "An underactuated adaptive 3d printed robotic gripper," in *Proc. 10th France-Japan/ 8th Europe-Asia Congress on Mechatronics*, 2014, pp. 110–115.

[4] L. A. A. Demers and C. Gosselin, "Kinematic design of an ejection-free underactuated anthropomorphic finger," in *Proc. IEEE Int. Conf. on Robotics and Automation*, 2009, pp. 2086–2091.

[5] M. G. Catalano, G. Grioli, A. Serio, E. Farnioli, C. Piazza, and A. Bicchi, "Adaptive synergies for a humanoid robot hand," in *Proc. IEEE-RAS Int. Conf. on Humanoid Robots*, 2012, pp. 7–14.

[6] L. U. Odhner and A. M. Dollar, "Dexterous manipulation with underactuated elastic hands," in *Proc. IEEE Int. Conf. on Robotics and Automation*, 2011, pp. 5254–5260.

[7] D. Aukes, S. Kim, P. Garcia, A. Edsinger, and M. R. Cutkosky, "Selectively compliant underactuated hand for mobile manipulation," in *Proc. IEEE Int. Conf. on Robotics and Automation*, 2012, pp. 2824–2829.

[8] L. U. Odhner, L. P. Jentoft, M. R. Claffee, N. Corson, Y. Tenzer, R. R. Ma, M. Buehler, R. Kohout, R. D. Howe, and A. M. Dollar, "A compliant, underactuated hand for robust manipulation," *The International Journal of Robotics Research*, vol. 33, no. 5, pp. 736–752, Apr. 2014.

[9] C. Melchiorri, G. Palli, G. Berselli, and G. Vassura, "Development of the UB hand IV: Overview of design solutions and enabling technologies," *IEEE Robotics and Automation Magazine*, vol. 20, no. 3, pp. 72–81, 2013.

[10] F. Lotti, P. Tiezzi, G. Vassura, L. Biagiotti, G. Palli, and C. Melchiorri, "Development of UB hand 3: Early results," in *Proc. IEEE Int. Conf. on Robotics and Automation*, 2005, pp. 4488–4493.

[11] M. Baril, T. Lalibert, C. Gosselin, and F. Routhier, "On the Design of a Mechanically Programmable Underactuated Anthropomorphic Prosthetic Gripper," *Journal of Mechanical Design*, vol. 135, no. 12, p. 121008, Oct. 2013.

[12] A. Dollar and R. Howe, "A robust compliant grasper via shape deposition manufacturing," *IEEE/ASME Trans. on Mechatronics*, vol. 11, no. 2, pp. 154–161, April 2006.

[13] U. Scarcia, G. Berselli, C. Melchiorri, M. Ghinelli, and G. Palli, "Optimal design of 3d printed spiral torsion springs," in *Proc. ASME Conf. on Smart Materials, Adaptive Structures and Intelligent Systems*, vol. 1, 2016.

[14] *Handbook of Spring Design*. Spring Manufacturers Institute, 2002.

[15] L. Xie, P. Ko, and R. Du, "The mechanics of spiral springs and its application in timekeeping," *ASME Journal of Applied Mechanics*, vol. 81, no. 3, pp. 034 504–034 504–7, 2013.

[16] L. Novakova-Marcincinova, J. Novak-Marcincin, J. Barna, and J. Torok, "Special materials used in fdm rapid prototyping technology application," in *2012 IEEE 16th International Conference on Intelligent Engineering Systems (INES)*, 2012, pp. 73–76.

[17] L. Howell, *Compliant Mechanisms*. John Wiley and Sons, 2001.

[18] ABSplus-P430 Production Grade Thermoplastic for Design Series 3D Printers. [Online]. Available: http://usglobalimages.stratasys.com/Main/Files/Material_Spec_Sheets/MSS_FDM_ABSplusP430.pdf

[19] G. Palli, G. Borghesan, and C. Melchiorri, "Modeling, identification and control of tendon-based actuation systems," *IEEE Trans. on Robotics*, vol. 28, no. 2, pp. 277–290, 2012.